Pergamon

Int. J. Solids Structures Vol. 34, No. 24, pp. 3141–3161, 1997

0020-7683/97 $17.00 + .00

PII: S0020-7683(96)00137-0

A 3D NUMERICAL STUDY OF DUCTILE TEARING AND FATIGUE CRACK GROWTH UNDER NOMINAL CYCLIC PLASTICITY

B. SKALLERUD and Z. L. ZHANG
Division of Applied Mechanics, The Norwegian Institute of Technology, N-7034, Trondheim, Norway and Sintef Materials Technology, N-7034, Trondheim, Norway

(*Received* 6 *October* 1995; *in revised form* 28 *June* 1996)

Abstract—Structures subjected to severe cyclic loading may fail due to low cycle fatigue. During the latter part of the fatigue life the crack growth rate may increase due to the occurence of crack growth from static failure modes, e.g. void growth. The present investigation attempts to predict the combined crack growth by means of nonlinear FE methods. The case studied is an axially loaded flat plate with embedded, nearly circular cracks growing under nominal cyclic plasticity, as test data for this case has been obtained previously. The fatigue part of the crack growth is determined by using the computed cyclic J-integral and the static mode crack growth from ductile tearing is determined from computations accounting for void nucleation/growth/coalescence by means of a modified Gurson–Tvergaard model. Comparison with the test results shows acceptable correspondence. © 1997 Elsevier Science Ltd.

INTRODUCTION

In typical fatigue loading, the structural life consists mainly of loading corresponding to high cycle fatigue. In some structures the operational loads may contain cycles in the fully plastic regime, i.e. low cycle fatigue. Additionally, structures designed according to high cycle fatigue criteria may be subjected to accidental loads or extreme environmental loads (waves, earthquakes), leading to low cycle fatigue damage (Skallerud *et al.*, 1995). Due to the intense loading in cyclic plasticity, the high maximum tensile loads may also lead to ductile tearing crack growth when the crack has reached a certain size. Most research in the past addresses these topics separately. In the present investigation cyclic elastic-plastic crack growth is analysed by means of nonlinear FE methods. The case analysed is an axially loaded plate with embedded, approximately circular cracks, as some test data have been obtained previously (Skallerud, 1992a). The fatigue crack growth is predicted by extension of the J-integral (Rice, 1968) to cyclic loading, ΔJ (Dowling and Begley, 1976) followed by application of this parameter in a fatigue crack growth model. As the crack geometry is simple, solution from an analytical study is also utilised for comparison. The ductile tearing is predicted from the Gurson–Tvergaard model (denoted G–T model subsequently), i.e. a porous material model representative for ductile damage (Gurson, 1977; Tvergaard, 1981, 1982). A refined failure criterion by Zhang and Niemi (1995a), based on a void coalescence mechanism, has been used in the fitting of the damage parameters. All numerical simulations were carried out with the ABAQUS software and the UMAT subroutine facility is employed for the implementation of the G–T model with the refined failure criterion (Zhang, 1995b).

Although experimentally determined crack growth curves for fatigue and tearing (separately) have been presented in the literature for different materials and cracked components, at present purely numerically determined crack growth curves are being successfully computed by means of micromechanical models (Xia and Shih, 1995). Hence, the potential of using micromechanical damage models in numerical analysis is approaching a firm basis. A numerical approach is beneficial in order to account for geometry effects on crack growth. The present investigation follows this line of method.

In the following, first some semi-empirical fatigue crack growth models and the micromechanical model are discussed. The FE formulation and modelling are presented, with

details of the G–T model parameter calibration. Finally, the FE results for the component with embedded, circular cracks subjected to cyclic plasticity are shown and discussed.

DAMAGE MECHANISMS AND MODELS IN FATIGUE AND DUCTILE TEARING

Fatigue

The intention of this section is not to summarize the large body of work done in fatigue research, see McEvily (1982) and Tanaka (1989) for excellent reviews. The intention is to point out some theories and models relevant for the present context.

In small scale yielding conditions the relationship between the J-integral for linear elastic materials and the Mode I stress intensity factor reads

$$J_e = K_I^2/E' \Rightarrow K_{I,J} = \sqrt{E'J_e}$$
$$E' = \left[\frac{E}{1-\nu^2}\Big|_{P\varepsilon}, \quad E\,|_{P\sigma}\right]. \tag{1}$$

The crack tip opening displacement relates to J as:

$$J = m\sigma_y\delta_{\text{tip}}. \tag{2}$$

Here, m is a constraint factor close to 1 in plane stress and approximately 2 in plane strain, for low hardening materials, presuming that J characterises the crack tip stress–strain field (HRR field) (Shih, 1981; Hutchinson, 1968; Rice and Rosengren, 1968).

In cyclic loading under small scale yielding, unloading from $\sigma_{\max}$ to $\sigma_{\min}$ (without crack closure) governs the change in δ_{tip} according to the following relationship (Rice, 1967)

$$\delta_{\text{tip}} \propto K_I^2/E'\sigma_y$$
$$\Delta\delta_{\text{tip}} \propto (\Delta K)^2/(E'2\sigma_y)$$
$$\Delta K = K_{\max} - K_{\min} \propto (\sigma_{\max} - \sigma_{\min})\sqrt{\pi a}. \tag{3}$$

The crack tip blunting model is one way of describing fatigue damage. It is based on the cyclic process of blunting and resharpening of the crack tip (Laird and Smith, 1962; Neumann 1974). A result from this model is that the crack advance is proportional to $\Delta\delta_{\text{tip}}$. The striation mechanism with crack advance in each cycle then leads to the following crack growth model:

$$\mathrm{d}a/\mathrm{d}N \propto (\Delta K)^2. \tag{4}$$

Detailed studies of structural steel show that this model may be valid for relatively high crack growth rates, although still under small scale yielding (Roven and Nes, 1991), whereas a semi-empirical model has to be utilised for lower rates (Paris and Erdogan, 1963):

$$\mathrm{d}a/\mathrm{d}N = \mathrm{C}_1(\Delta\mathrm{K})^{n_1}. \tag{5}$$

n_1 is typically between 2 and 4, and close to 3 for structural steel. Figure 1(a) illustrates schematically typical fatigue crack growth rates in log–log axes. For high cyclic loading in the ligament (due to a large crack or small crack/high nominal load), the small scale yielding parameter K_I is invalidated. Now the J-integral is a possible parameter for describing control of the crack tip damage process zone. J is derived for a nonlinear elastic (deformation plastic) material (Rice, 1968) and may be written as the sum of an elastic and a plastic contribution (Shih and Hutchinson, 1976):

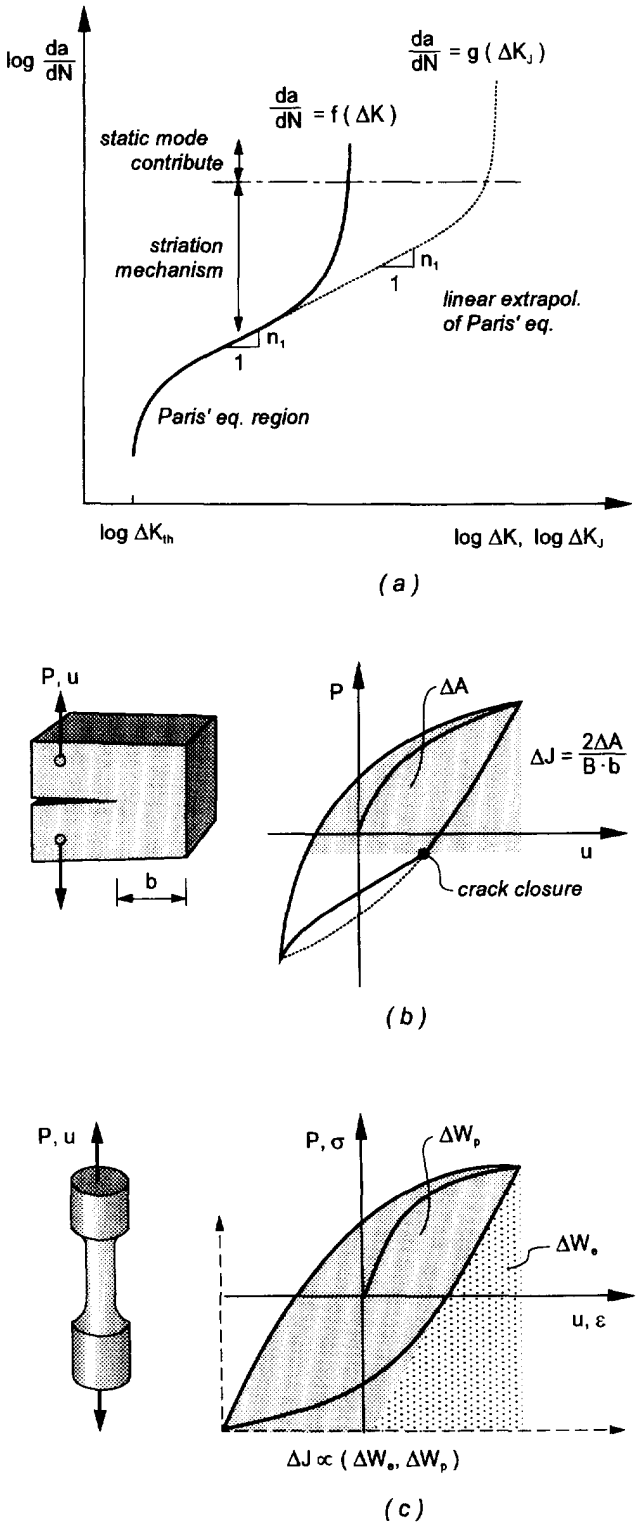

Fig. 1. (a) Crack growth rate behaviour; (b) ΔJ determination (significant crack closure); (c) ΔJ determination (insignificant crack closure).

$$J = \int_\Gamma \left(Wn_1 - \mathbf{t} \cdot \frac{\partial \mathbf{u}}{\partial x_1} \right) \mathrm{d}s \approx J_e + J_p \tag{6}$$

$$W = \int_0^\varepsilon \boldsymbol{\sigma} : \mathrm{d}\boldsymbol{\varepsilon}, \quad \boldsymbol{\sigma} = \frac{\partial W}{\partial \boldsymbol{\varepsilon}}. \tag{7}$$

Although application of J in cyclic loading does not have a theoretical basis as for monotonic loading, it is still a relevant candidate for correlation of fatigue crack growth under large scale yielding. One could assume that the cyclic plastic crack growth was proportional to the energy dissipated per cycle at the crack tip. Then the requirement for proportional straining of the material necessary for the J-integral could be abandoned. This approach requires a fine FE mesh. However, the link between K and J shown below is convenient in estimation of fatigue crack growth parameters. Dowling (1978) utilised the connection between J and the elastic and plastic strain energy in cyclic loading for axially loaded specimens, where the strain energy in a cycle was taken as the area under the stress–strain curve starting at $(\sigma_{\min}, \varepsilon_{\min})$ and ending at $(\sigma_{\max}, \varepsilon_{\max})$. This approach presumes insignificant effects of crack closure. Describing the loading branch by a doubled Ramberg–Osgood curve according to the Masing-hypothesis (Masing, 1926), an estimate for ΔJ could be obtained from the area under the loading branch of the curve:

$$\Delta J = F_{g,el} \Delta W_e a + F_p(a, n) \Delta W_p a \tag{8}$$

$$\Delta K_J = \sqrt{E' \Delta J}. \tag{9}$$

The F factors account for finite geometry, crack shape and strain hardening and were derived in (Shih and Hutchinson, 1976) for monotonic loading. Note that the energies should account for eventual effects of crack closure, i.e. ΔJ is effective. Figure 1(b) illustrates the operational ΔJ obtained from load–displacement curves with significant crack closure, whereas Fig. 1(c) depicts a load–displacement (or stress–strain) curve for a specimen without significant crack closure (e.g. in a cylindrical, axially loaded LCF specimen). By correlating ΔK_J to the low cycle fatigue crack growth, a linear relationship was obtained in log-log axes, located in the extrapolated Paris' region (Dowling and Iyyer, 1987; McClung and Hudak, 1994; Joyce *et al.*, 1994):

$$\mathrm{d}a/\mathrm{d}N = C_2(\Delta K_J)^{n_2} \approx C_1(\Delta K_J)^{n_1}. \tag{10}$$

The definition of ΔJ is (Tanaka, 1989):

$$\begin{aligned} \Delta J &= \int_\Gamma \left(\Delta W n_1 - \Delta \mathbf{t} \cdot \frac{\partial \Delta \mathbf{u}}{\partial x_1} \right) \mathrm{d}s \\ &\approx \Delta J_e + \Delta J_p \\ \Delta W &= \int_{\varepsilon_{\min}}^{\varepsilon_{\max}} (\boldsymbol{\sigma} - \boldsymbol{\sigma}_{\min}) : \mathrm{d}\boldsymbol{\varepsilon}, \\ \Delta \boldsymbol{\sigma} &= \frac{\partial \Delta W(\Delta \boldsymbol{\varepsilon})}{\partial \Delta \boldsymbol{\varepsilon}}, \quad \Delta \mathbf{t} = \mathbf{t}_{\max} - \mathbf{t}_{\min}. \end{aligned} \tag{11}$$

Equation (11) is only valid for a stabilized material response (Yoon and Saxena, 1991) i.e. cyclic hardening/softening is saturated. For the steel analysed subsequently this transient material behaviour is moderate and saturation quite rapid (Skallerud, 1992b). Hence, in this respect the ΔJ determination should be acceptable. Note that $\Delta J \neq J_{\max} - J_{\min}$, but is obtained by developing eqn (11)

$$\Delta J = J_{\max} - J_{\min} - \int_{\Gamma} \left(\boldsymbol{\sigma}_{\min} : (\boldsymbol{\varepsilon}_{\max} - \boldsymbol{\varepsilon}_{\min}) n_1 - \mathbf{t}_{\max} \cdot \frac{\partial \mathbf{u}_{\min}}{\partial x_1} + \mathbf{t}_{\min} \cdot \frac{\partial \mathbf{u}_{\max}}{\partial x_1} \right) \mathrm{d}s. \tag{12}$$

This means that the computed $J_{\max}$, $J_{\min}$ by means of eqn (6) or the virtual crack extension method implemented in ABAQUS is not feasible. The only implementation of eqn (11) known to the authors has been performed by Lambert *et al.* (1988), where the results computed corresponded well with ΔJ values both calculated from the load–displacement curves in tests and the numerically determined load–displacement curves, hence according to the area under the loading part of the load–displacement curve, see Fig. 1(b) and (c). A way of utilising the results from ABAQUS for ΔJ determination is presented subsequently.

Considering Fig. 1(a), for a further increase in ΔK_J, the log–linear relationship breaks down and an increase in crack growth rate develops. This increase may be attributed to static fracture modes, e.g. from ductile tearing. Previous studies show that for some materials the interaction between the fatigue mode and static modes is negligible (Kaiser, 1983; Chell, 1984; Neale and Priddle, 1988), and the increased crack growth due to ductile tearing may be simulated by an amplification factor obtained from a monotonic J_R curve:

$$\mathrm{d}a/\mathrm{d}N = \mathrm{d}a/\mathrm{d}N\,|_{\text{fatigue}} + \mathrm{d}a/\mathrm{d}N\,|_{\text{tearing}} \tag{13}$$

$$\Rightarrow \mathrm{d}a/\mathrm{d}N = C_3(\Delta J)^{n_3} \Big/ \left(1 - \frac{T_{\max}}{T_{\mathrm{mat}}}\right) \tag{14}$$

$$\frac{T_{\max}}{T_{\mathrm{mat}}} = \frac{\mathrm{d}J_{\max}/\mathrm{d}a}{\mathrm{d}J_{\mathrm{mat}}/\mathrm{d}a}.$$

By this method the upturn of the $\mathrm{d}a/\mathrm{d}N - \Delta K$ curve, Fig. 1(a), is obtained.

Ductile tearing

Equation (14) is only utilised herein for discussion purposes. Instead, as the damage process in ductile tearing usually consists of void nucleation/growth/coalescence, a micro-mechanical model originally proposed by Gurson (1977) and later modified by Tvergaard (1981) and Tvergaard and Needleman (1984), is employed with some modifications. By assuming that the matrix material is characterised by a Mises material and the void shape is kept spherical, using upper bound theory, Gurson derived a plastic potential for a voided solid that returns to the Mises yield surface for zero void volume fraction:

$$\Phi(\boldsymbol{\sigma}, f, \bar{\sigma}) = \frac{q^2}{\bar{\sigma}^2} + 2q_1 f \cosh\left(\frac{3q_2\sigma_m}{2\bar{\sigma}}\right) - 1 - (q_1 f)^2 = 0$$

$$q^2 = \tfrac{3}{2}\mathbf{s}:\mathbf{s}, \quad \mathbf{s} = \boldsymbol{\sigma} - \sigma_m \mathbf{I}, \quad \sigma_m = \tfrac{1}{3}\boldsymbol{\sigma}:\mathbf{I}. \tag{15}$$

Here f is the void volume fraction, $\bar{\sigma}$ is the matrix material yield stress, $q_1 = 1.5$ and $q_2 = 1$ are parameters introduced by Tvergaard for better correspondence to FE results, $\boldsymbol{\sigma}$ is the Cauchy stress tensor, $\mathbf{I}$ is the second-order unit tensor.

During loading the void volume fraction increase is governed by:

$$\mathrm{d}f = \mathrm{d}f_{\text{nucleation}} + \mathrm{d}f_{\text{growth}}$$

$$\mathrm{d}f_{\text{growth}} = (1-f)\,\mathrm{d}\boldsymbol{\varepsilon}^{\mathrm{p}} : \mathbf{I}$$

$$\mathrm{d}f_{\text{nucleation}} = A\,d\bar{\varepsilon}^{\mathrm{p}} \tag{16}$$

where $\boldsymbol{\varepsilon}^{\mathrm{p}}$ is the overall plastic strain tensor and $d\bar{\varepsilon}^{\mathrm{p}}$ is the equivalent plastic strain increment. Here a strain controlled nucleation criterion has been applied. The void nucleation parameter A may be described by the normal distribution model (Chu and Needleman, 1980):

$$A = \frac{f_N}{s_N\sqrt{2\pi}} \exp\left[-0.5\left(\frac{\bar{\varepsilon}^p - \varepsilon_N}{s_N}\right)^2\right]. \tag{17}$$

The parameters are defined subsequently in the calibration section. By equivalence of overall and matrix plastic work, the equivalent plastic strain increment controlling matrix hardening reads

$$d\bar{\varepsilon}^p = \frac{\boldsymbol{\sigma} : \mathbf{d}\varepsilon^p}{(1-f)\bar{\sigma}}. \tag{18}$$

The overall plastic strain increment is given by the associated flow rule $d\varepsilon^p = \mathrm{d}\lambda\partial\Phi/\partial\boldsymbol{\sigma}$. The Gurson model itself is not able to predict the void coalescence. An extra criterion for void coalescence should be used. To account for this, f is replaced by f^* in eqn (15). f^* equals f for $f \leqslant f_c$ and $f_c + [(f_u^* - f_c)/(f_F^* - f_c)](f - f_c)$ otherwise. Note that a failure criterion is inherent, namely the void volume fraction at coalescence, f_c, and it is determined by numerical simulations of simple tensile tests. Zhang and Niemi (1995a) modified f_c, taking it to be the value of f when a void coalescence criterion, based on Thomason's localisation criterion (Thomason, 1989), is fulfilled. Hence, a physical criterion is employed.

Some experimental observations

In the investigation by Skallerud (1992a), the test specimen shown in Fig. 2 was used. It is a flat plate buttwelded at midsection. The base material is of type St52-3N, a normalised CMn structural steel typically applied in the offshore industry. The monotonic and cyclic stress–strain curves are plotted in Fig. 3. The weld matched the base material. The chemical compositions of the materials are listed in Table 1.

The testing was carried out in fully reversed axial loading, with the base metal nominal axial strain as controlling parameter, analogous to LCF testing of cylindrical specimens. The strain was monitored by means of clip gages with a measurement length of 10 mm. None of the specimens contained fatigue precracks.

Although the crack initiated and grew differently among the 10 plates tested, the crack growth rate could be correlated to the nominal strain amplitude as

$$\mathrm{d}a/\mathrm{d}N = 35\,600\varepsilon_a^{3.09} a \tag{19}$$

$$\ln a = N35\,600\varepsilon_a^{3.09} + \ln a_0. \tag{20}$$

An initial crack size of 0.1 mm is employed in eqn (19). Two of the specimens developed cracks growing from a weld root inclusion as an embedded, approximately circular crack. The micrographs in Fig. 4 show one of the crack surfaces, with clear striation patterns. Here the nominal strain amplitude was 1.3% and the number of cycles to failure was 80. The insets show the fracture surfaces at ≈ 1 and 7 mm, respectively. For the smallest crack, no sign of dimples representing necking between voids is observed, whereas for the large crack dimples clearly are visible. Figure 5 shows the comparison between the measured crack growth for this specimen and that predicted by eqn (19).

In the following it is attempted to predict $\mathrm{d}a/\mathrm{d}N$ from fatigue and ductile tearing contributions by means of computed values of fatigue and tearing crack growth according to eqn (13). The specimen described above is used in all simulations, as it has a well defined crack shape and growth behaviour.

FE FORMULATION AND MODELLING

Large deformations are accounted for in all analyses, i.e. an updated Lagrangian type formulation combined with the algorithm presented by Hughes and Winget (1980) accounting for large rigid body rotations (Hibbitt *et al.*, 1992). The strain measure is based

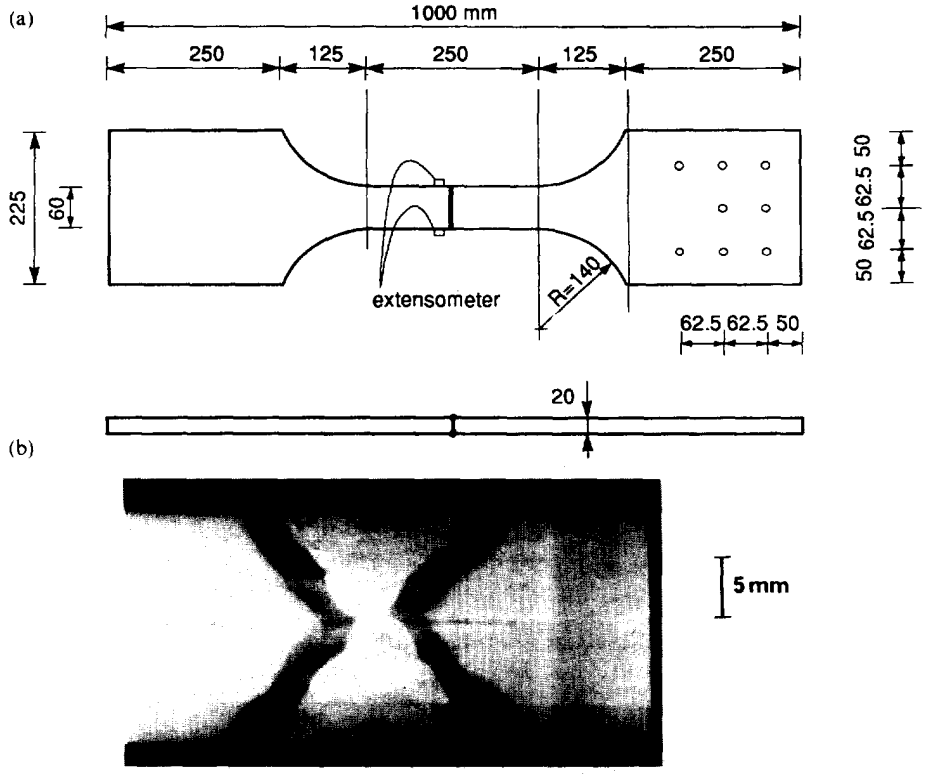

Fig. 2. Test specimen and buttweld geometry.

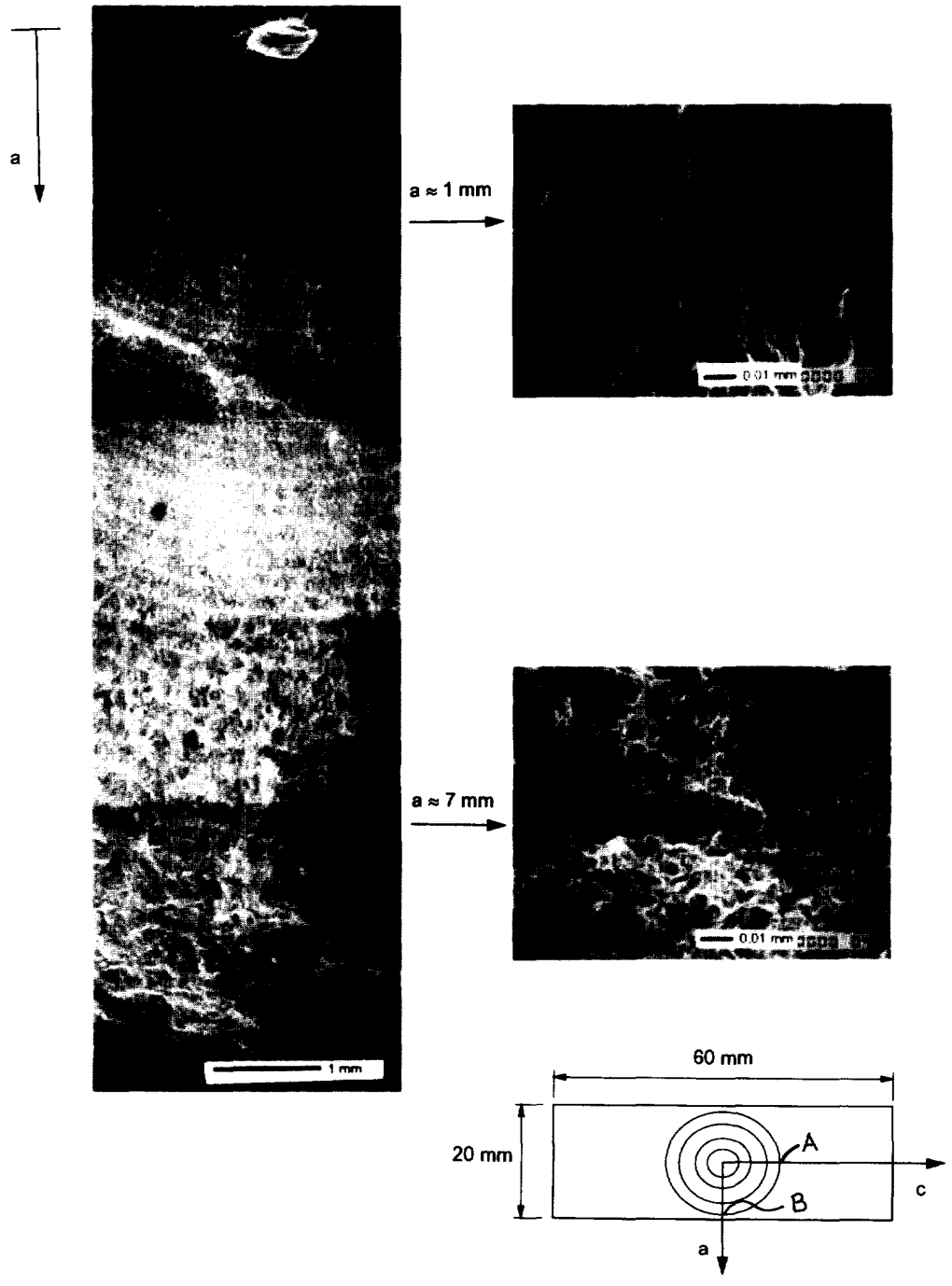

Fig. 4. Striation pattern and crack surface details.

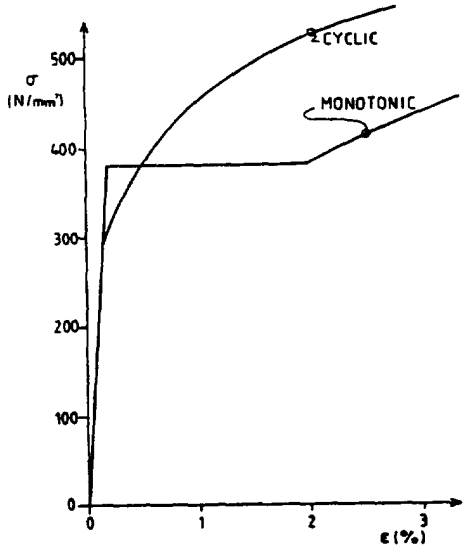

Fig. 3. Monotonic and cyclic stress–strain curve.

Table 1. Chemical composition (%wt) and mechanical properties data for base and weld metal

	C	Si	Mn	P	S	Cu	Ni
Base metal	0.19	0.39	1.49	0.013	0.007	0.01	0.03
Weld metal	0.08	0.35	0.91	0.014	0.007	0.01	0.01
	Cr	Mo	V	Ti	Nb	Al	H
Base metal	0.02	0.01	0.01	0.001	0.002	0.035	0.00009
Weld metal	0.03	0.01	0.02	0.02	0.003	0.002	0.00005

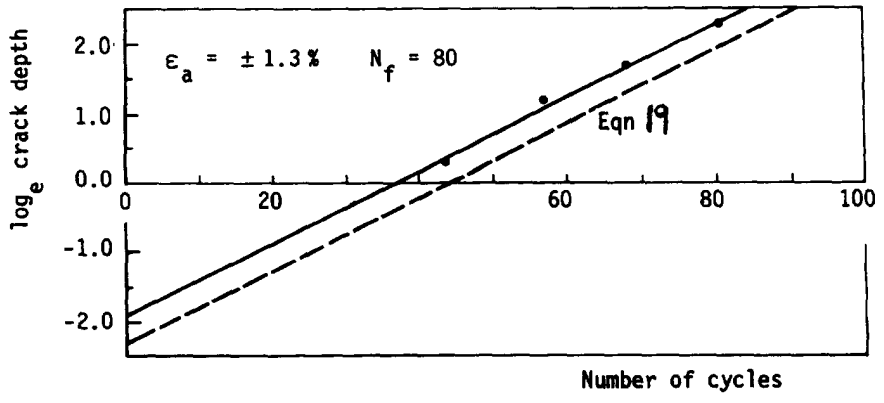

Fig. 5. Crack depth (a) vs cycles.

on the rate of deformation, and is combined with the Jaumann rate of the Kirchoff stress yielding a stress increment without rigid body contributions for an infinitesimal time increment, i.e. $\hat{\boldsymbol{\tau}} = \mathbf{C}^{ep} : \mathbf{D}$, ($\mathbf{D} = \text{symm}\partial(\partial\mathbf{x}/\partial t)/\partial\mathbf{x}$, $\mathbf{W} = \text{antisymm}\partial(\partial\mathbf{x}/\partial t)/\partial\mathbf{x}$, $\hat{\boldsymbol{\tau}} = \dot{\boldsymbol{\tau}} - \mathbf{W}\boldsymbol{\tau} + \boldsymbol{\tau}\mathbf{W}$, $\boldsymbol{\tau} = |\,\partial\mathbf{x}/\partial\mathbf{X}\,|\,\boldsymbol{\sigma}$, $\mathbf{x}$ is the current position of a material point, $\mathbf{X}$ is the reference position).

In the tearing analyses the large deformations are important due to the intense straining at the crack tip and the simultaneous void nucleation/growth/coalescence. Utilising the G–T model in the FE analyses, hence accounting for the voids, the tangent stiffness at an integration point provides a vanishing stress carrying capability after void coalescence and tearing is simulated element by element for increasing external loading. The continuum expression for the tangent stiffness reads:

$$\hat{\tau}_{ij} = C^{ep}_{ijkl} : D_{kl} \forall \left(\Phi = 0, \hat{\sigma} : \frac{\partial \Phi}{\partial \sigma} > 0 \right) \tag{21}$$

$$C^{ep}_{ijkl} = \frac{E}{1+v}\left(\delta_{ik}\delta_{jl} + \frac{v}{1-2v}\delta_{ij}\delta_{kl} - \frac{P_{ij}P_{kl}}{\bar{E}} \right) \tag{22}$$

$$P_{ij} = \frac{3}{2}\frac{s_{ij}}{\bar{\sigma}} + \eta \frac{1+v}{1-2v}\delta_{ij}$$

$$\eta = \frac{f}{2} q_1 q_2 \sinh \frac{3q_2\sigma_m}{2\bar{\sigma}}$$

$$\bar{E} = (1+v)\frac{\bar{H}}{E} + \frac{3q^2}{2\bar{\sigma}^2} + 3\eta^2 \frac{1+v}{1-2v}$$

$$\bar{H} = -\frac{\bar{\sigma}}{2}\left[3\eta(1-f)\frac{\partial \Phi}{\partial f} + \left(\frac{\partial \Phi}{\partial \bar{\sigma}} + A\bar{h}\frac{\partial \Phi}{\partial f} \right)\left(\frac{q^2}{\bar{\sigma}^2} - \eta \frac{3q_2\sigma_m}{2\bar{\sigma}} \right)\frac{\bar{h}}{1-f} \right]$$

$$\bar{h} = \mathrm{d}\bar{\sigma}/\mathrm{d}\bar{\varepsilon}^p.$$

The constitutive equations were implemented via the user material facility in ABAQUS by means of the backward Euler integration method. A consistent tangent operator was utilised, hence the quadratic rate of convergence in the Newton method solving the global equilibrium was preserved. Confer Zhang and Niemi (1995b) and Zhang (1995b) for details.

In the cyclic analyses a bi-linear kinematic hardening model as implemented in ABAQUS is applied. The continuum expression reads:

$$\hat{\tau}_{ij} = \frac{E}{1+v}\left[\delta_{ik}\delta_{jl} + \frac{v}{1-2v}\delta_{ij}\delta_{kl} - \frac{3(s_{ij}-\alpha^*_{ij})(s_{kl}-\alpha^*_{kl})}{2\sigma_y^2\left(1+\frac{\bar{h}}{3G}\right)} \right] D_{kl}. \tag{23}$$

Here α^*_{kl} represents the deviatoric part of the back stress tensor and G is the shear modulus. $\sigma_y = 360$ MPa and $\bar{h} = 2200$ MPa were applied as an approximate description of the cyclic stress–strain behaviour. This represents closing of the hysteresis loops and contains no transient material behaviour. Modelling of the transient behaviour is given in (Skallerud, 1992b). Therefore, the ΔJ approach is acceptable. Although the ABAQUS theory manual points out caution in using this material model for strains larger than 25% due to plasticity induced anisotropy, the cyclic loading analysed herein did not lead to such high strain levels except at the crack tip. Here, however, the stress–strain results were not utilised in the analysis of fatigue crack growth.

Initially some plane strain analyses were carried out. These did not give acceptable results (too much strain concentration in the ligament, and too high constraint at the crack tip leading to large overprediction of ductile tearing). Therefore, it was decided to run three-dimensional analyses of the component. Due to symmetries, only 1/8 of the specimen was modelled. The crack sizes analysed subsequently are $a = c = 3$, 5, 6, 7 and 8 mm, respectively. The local mesh arrangements in the crack tip region for the five models are exactly the same. Figure 6 illustrates the FE mesh for $a = c = 5$ mm. The size of the brick elements at the crack tip, and in the prospective crack growth direction, was 0.033 mm. In most cases 20 noded solid elements with reduced integration ($2 \times 2 \times 2$ Gauss points) were applied. In the cyclic analyses the same mesh, but with eight-noded solid elements instead, was used due to computer time consumption. In the cyclic analyses uniaxial gap elements were used at the crack surface. Hence, the numerical results accounted for crack opening and closure, and these effects could be monitored. The analyses were run in displacement control, with a boundary displacement amplitude corresponding to the nominal strain amplitude in the test.

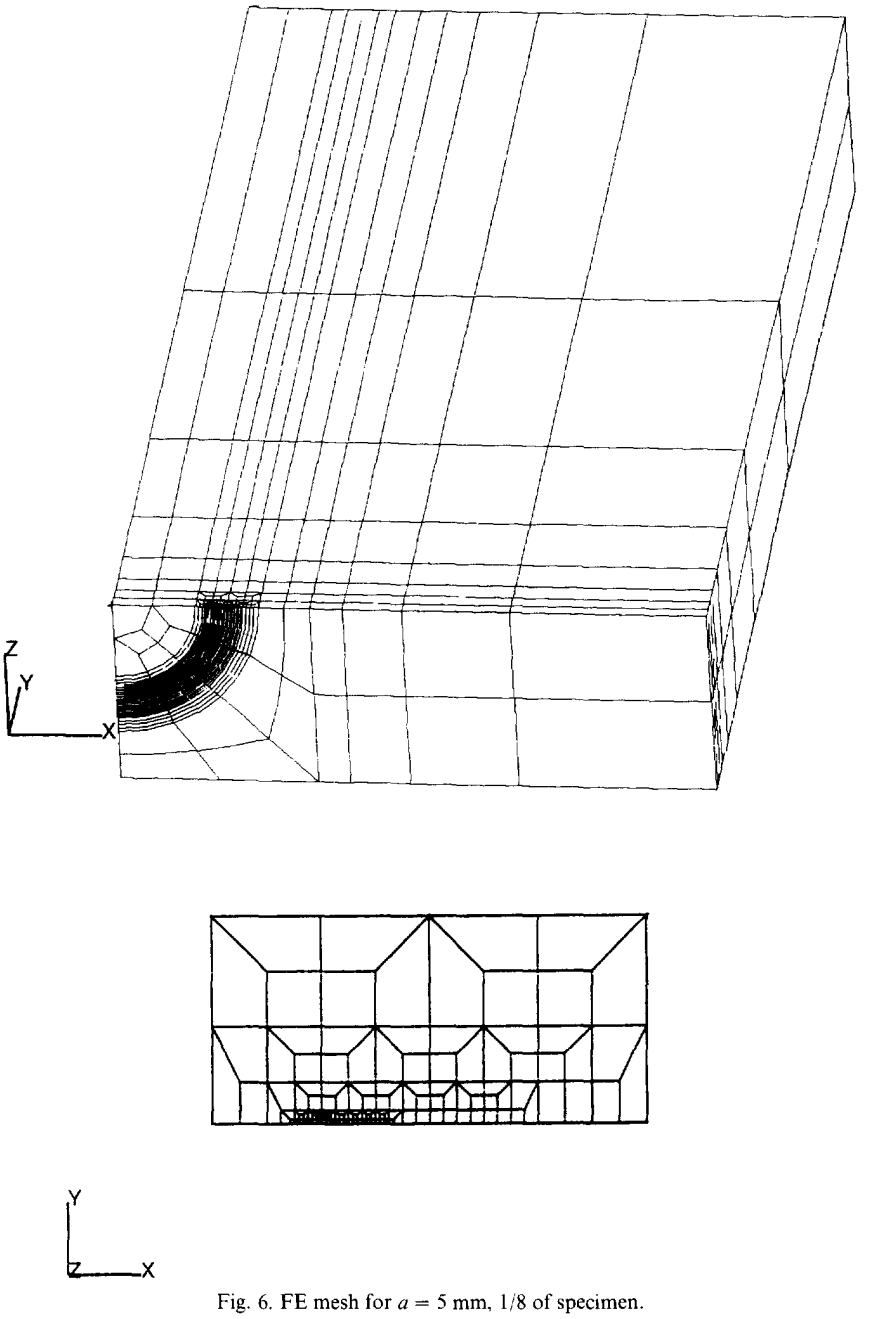

Fig. 6. FE mesh for $a = 5$ mm, 1/8 of specimen.

Calibration of the Gurson model parameters

One important aspect in the application of the G–T model is the establishment of the material parameters. Recently a methodology for determining the damage parameters has been proposed by Zhang (1995a) in which the parameters have been classified into four categories, the constitutive parameters (q_1 and q_2), the hardening parameters (true stress–strain curve), the initial material parameters (f_0 and the nucleation parameters) and the critical parameter (f_c). The constitutive parameters and hardening parameters are usually not the great concern of an application. In our case, $q_1 = 1.25$ and $q_2 = 1.0$ suggested by Koplik and Needleman (1988) were used. The great concern is how to determine or select the initial as well as critical parameters. By using the methodology which is based on Thomason's dual dilatational plasticity theory (Thomason, 1989) the initial as well as the critical parameters can be determined.

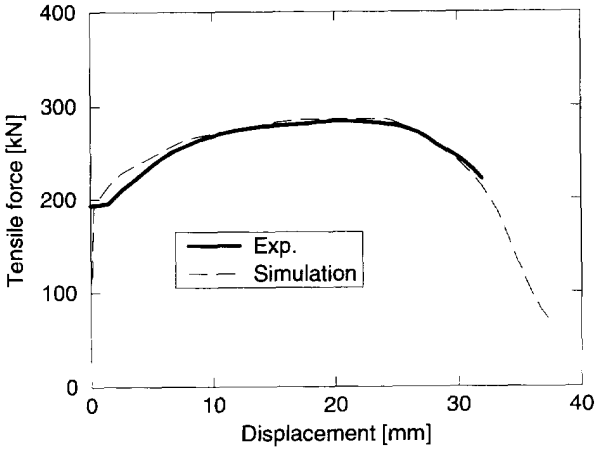

Fig. 7. Experimental and numerical load–displacement curve for tensile test.

In general, there are two families of voids in steel, corresponding to large inclusions and small carbides, which should be taken into account. The primary voids nucleated from large inclusions usually are assumed to be present (nucleated) at the beginning of plastic loading. Its void volume fraction f_0 can be approximately obtained from the inclusion MnS by Franklin's formula (Franklin, 1969):

$$f_r = 0.054\left[S(\%) - \frac{0.001}{Mn(\%)}\right]. \tag{24}$$

The chemical compositions of the steel and weld metal investigated in this paper are shown in Table 1. The calculated void volume fraction of MnS are 0.00034 and 0.00032 for the steel and its weld metal, respectively. In our FE analyses, the value $f_0 = 0.00033$ has been used.

The secondary voids nucleated from the small carbides during the plastic deformation are difficult to model accurately. Normally stress or strain controlled nucleation rules can be used. In this study, the strain-controlled nucleation rule by Chu and Needleman (1980) is applied, see eqn (17), in which ε_N is the mean nucleation strain for the small carbides, s_N is the standard deviation and f_N is the volume fraction of nucleating particles. In the literature, the values $\varepsilon_N = 0.3$, $s_N = 0.1$ proposed by Tvergaard and Needleman (1984) have been widely used and are also used in our analyses. The remaining unknowns f_N and f_c are fitted from the tensile tests. In the parameter fitting, several f_N values have been tried. Because a mechanism characterized by void coalescence has been employed, the material failure is automatically determined for a given f_N value. By comparing the numerical and experimental results, the value of $f_N = 0.006$ which gives best fit to the experimental results was chosen as the "true" volume fraction of the nucleating particles. The critical void volume fraction f_c which is a result of the parameter fitting, corresponding to $f_N = 0.006$, is 0.026. The value of f_F is not very critical for the analyses, and was chosen as 0.15. These values have been used in the following analyses. Figure 7 shows the numerical and experimental results for the tensile test.

NUMERICAL SIMULATIONS

Ductile tearing analyses

Five three-dimensional models with (circular) crack size $a = 3$, 5, 6, 7 and 8 mm have been analyzed with the established material parameters. Figure 6 shows the finite element mesh for the 5 mm crack. The dimensions of the model are $60 \cdot 30 \cdot 10$ mm. The local mesh arrangement at the crack tip is also presented in Fig. 6. As normal practice for ductile tearing analyses, uniform square elements have been used. There are 4368 nodes and 808

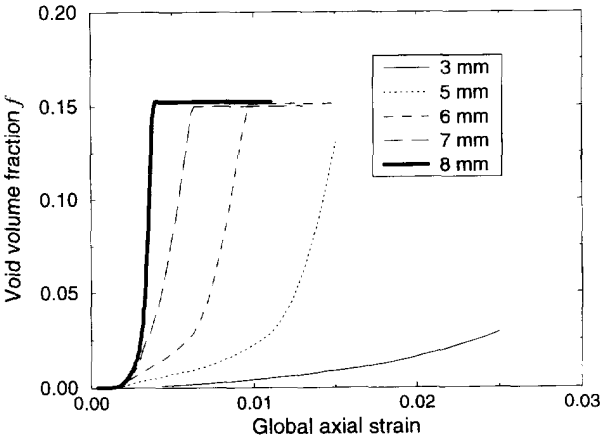

Fig. 8. Evolution of void volume fraction in near tip integration point (location A) for crack sizes $a = 3, 5, 6, 7, 8$ mm.

20-node elements in the 5 mm crack model. The number of elements and nodes for all crack models are similar to those in the 5 mm crack model.

The void volume fractions as a function of the nominal strain at the most critical integration point at crack tip location A (largest ligament) for the three models are compared in Fig. 8. It is interesting to note that for the 3 mm crack model, there is no crack growth even when the nominal strain is larger than 2%, however, according to the G–T model, the ductile tearing will start to appear when the nominal strain is about 0.5%. For the 5 mm crack model the ductile crack growth will start at the nominal strain 1.4%. In other words, according to the simulations the ductile tearing will begin to contribute to the total crack growth in the fatigue test when the crack size has reached 5 mm.

Figure 9 shows the ductile crack growth at location A (largest ligament) as a function of the nominal strain for the 5, 6, 7 and 8 mm crack models. In this study, the numerical crack is defined as the part of material in the crack plane where the loading capacity has "disappeared". In the analyses, in order to avoid numerical problems, a small amount of the loading capacity was remaining even when the crack had advanced. It can be found that once the crack has initiated, it grows faster in the 6/7/8 mm models than in the 5 mm model, probably because the a/w value at location A is larger for the 7 mm model than for the 5 mm. The crack growth for the 6, 7 and 8 mm models at the applied nominal strain amplitude 1.3 % is about 0.05, 0.15 and 0.45 mm, respectively.

The distribution of the averaged values of f at load levels which gives comparable f values around the crack front in the first element at the crack tip is shown in Fig. 10(a). It can be seen that in the 3 and 5 mm crack models, with the boundaries still relatively remote, the distribution is almost even at the crack front. However, the maximum f appears at

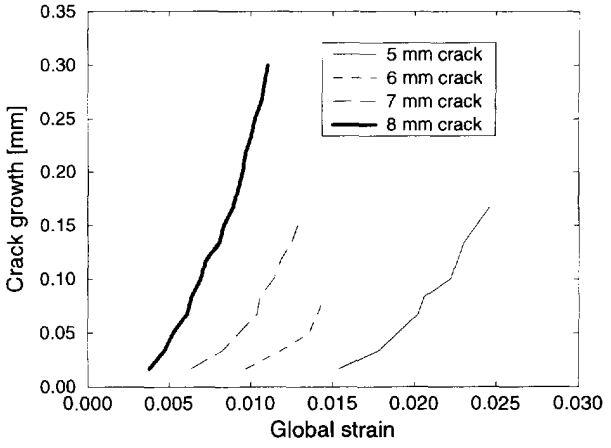

Fig. 9. Ductile tearing crack growth for location A.

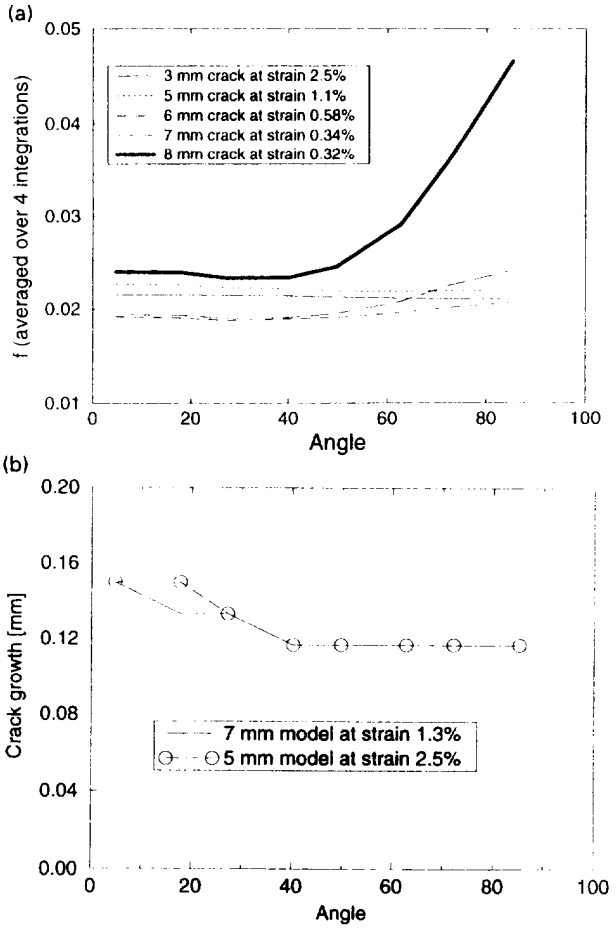

Fig. 10. Void volume fraction at crack front.

location B in the 6, 7 and 8 mm models. It means that crack growth will be initiated at location B. However, once the crack growth has started, the crack will grow more at A and less at B. Figure 10(b) indicates the crack growth along the crack front for the 7 mm crack model at 1.3% nominal strain and for the 5 mm crack model at 2.5% nominal strain.

Cyclic analyses

Figure 11(a) shows one (stable) computed load–displacement loop for the 5 mm crack specimen. It is observed that globally, no sign of crack closure is detected in this three-dimensional (3D) model. This complies with test results. Figure 11(b) shows the corresponding plot assuming plane strain, exhibiting significant crack closure. The explanation of the different response is simply the large difference in crack area versus net area, as the plane strain model has $a/w = 0.5$ (50% cracked surface) and the 3D model has 7% cracked surface.

Figure 12 illustrates by curve 1 the evolution of the load in the gap element nearest to the crack tip (location A in the 3D model) during 1.5 cycle for the 5 mm crack model. The force is zero as long as the crack is open, then just after unloading, this element makes contact. During further unloading this element force reduces slightly as the other gap elements come into contact. At (fictitious) time 1.0 the slope of the nominal load–displacement curve changes from negative to positive as the tensile excursion begins. Almost immediately the gap forces vanish, i.e. the crack opening load corresponds approximately to minimum load. This is in accordance with the study by Dowling and Iyyer (1987), showing low crack opening loads for axially loaded specimens tested in cyclic plasticity. Hence, it is reasonable to take the full loading branch into account when computing J-integrals (Fig. 1(c)). Curve 2 in Fig. 12 represents the gap element displacement. The

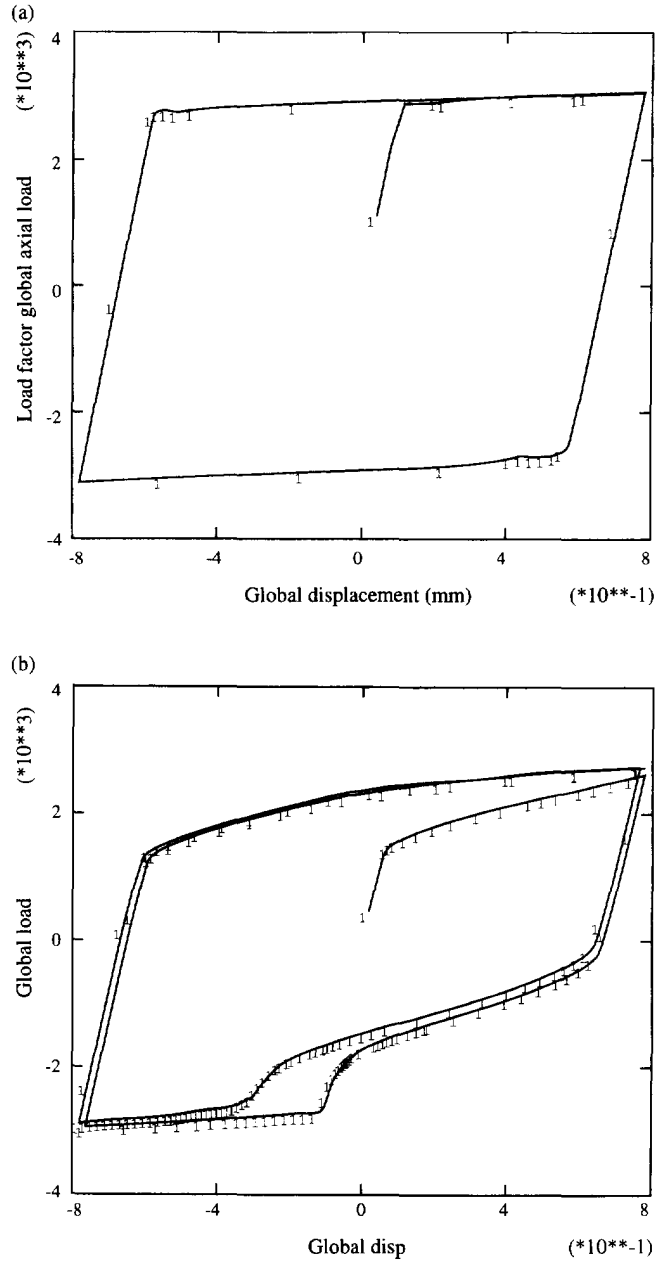

Fig. 11. (a) Load–displacement behaviour for $a = 5$ mm, 3D FE model; (b) load–displacement behaviour for $a = 5$ mm, plane strain FE model ($a/w = 0.5$).

simulations showed that after the first tensile excursion the gap element displacements saturated to constant values. Figure 12 shows a value of about 0.11 mm for the gap element nearest to the crack tip. Curve 3 is the boundary displacement history for the specimen.

Figure 13 illustrates the gap element displacements for crack center, intermediate distance from crack tip and the near tip element (curve 1), located 5, 2.5 and 0.05 mm from the crack tip location A, respectively. As $\Delta J \neq J_{max} - J_{min}$, the J-values obtained by ABAQUS during the cyclic loading could not be utilised. However, as the crack opens near the minimum load, a numerical ΔJ may be calculated by taking the doubled stress–strain curve as material model (Masing-hypothesis) and subject the cracked component to $2\varepsilon_a$ monotonically. This is analogous to the way the area under the load-displacement curve in cyclic loading is used in obtaining test result ΔJ, see Fig. 1(b) and (c) (Dowling, 1978; Lambert *et al.*, 1988). Using this method the J-integral evolution for the three crack sizes is plotted in Fig. 14. The x-axis is the fictitious analysis time, a similar evolution is exhibited

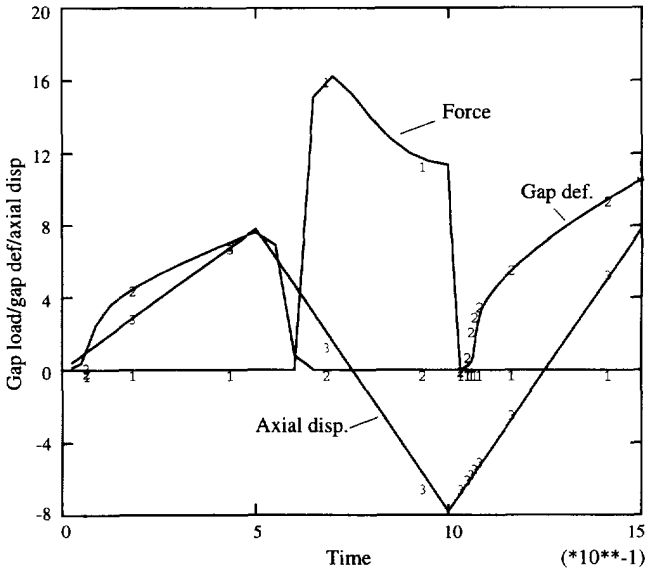

Fig. 12. Gap element behaviour for near tip element at location A.

in terms of nominal strain. Nine locations at the crack tip, each with six contours, were employed in calculation of J. Figure 14 shows the J-values at points A and B and some contour values for point A in order to assess path dependencies. The path dependency is small (but increasing for increasing crack size). It is interesting to note, however, that the J-value at point B is larger than at point A (largest ligament). For the 3, 5, 6, 7 and 8 mm cracks the following ΔJ values are obtained for point B: 150, 400, 594, 800 and 1100 N mm^{-1}, respectively.

Fitting the bilinear stress–strain curve to a Ramberg–Osgood curve, and exponent of 5.35 is determined for strains less than 0.03. Applying this curve in an estimation of J for the 3 mm crack, assuming that the effect of finite geometry is negligible, the following value is determined for the hysteresis loop governed by strain amplitude 0.013:

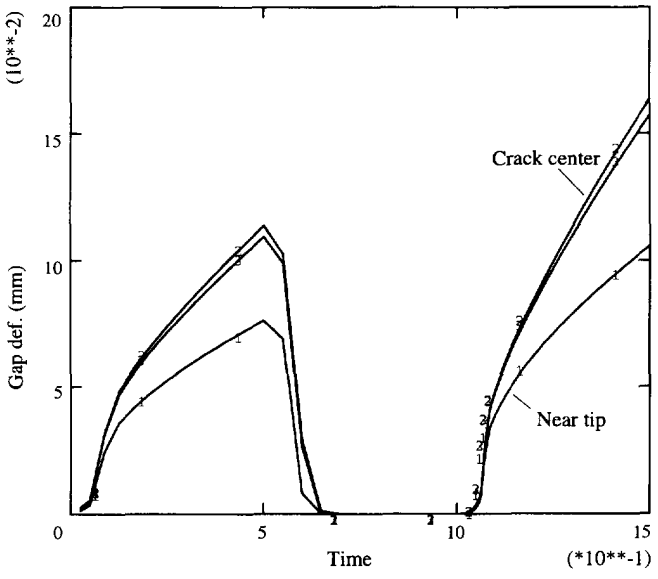

Fig. 13. History plot of gap deformations at crack centre, intermediate distance from crack tip, and near crack tip (location A).

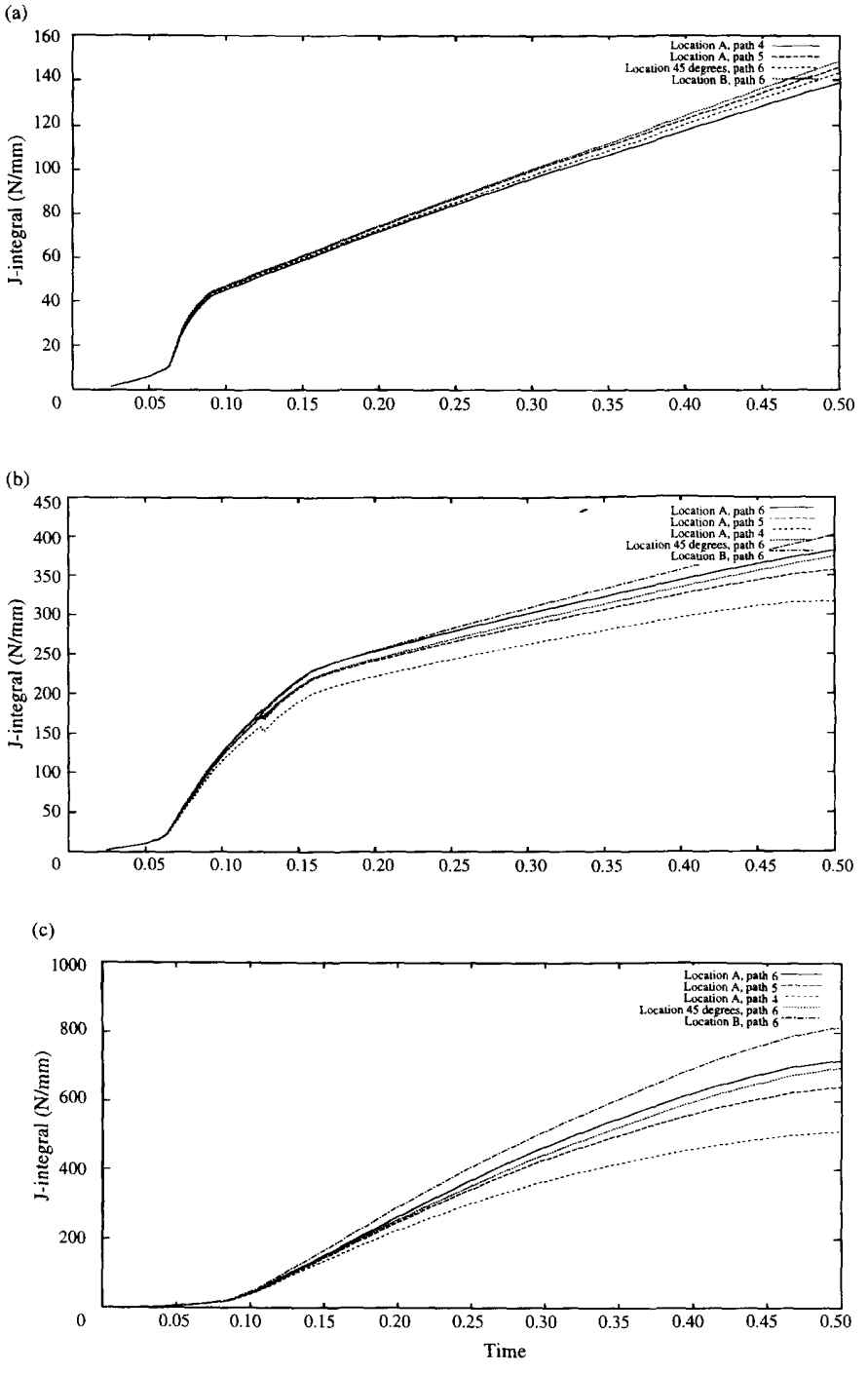

Fig. 14. J-evolution, 3D model: (a) $a = 3$ mm; (b) $a = 5$ mm; (c) $a = 7$ mm.

$$\Delta J = \Delta J_e + \Delta J_p = \frac{1}{E'}\left(\frac{2}{\pi}\Delta\sigma\sqrt{\pi a}\right)^2 + \left(\frac{2}{\pi}\right)^2 2\pi F(n)\Delta W_p a \approx 100\ \mathrm{N\,mm^{-1}}. \tag{25}$$

Here the same crack shape factor is assumed in the plastic term also. Neglecting this factor in the plastic term, $\Delta J \approx 250$ N mm^{-1}. The hardening factor $F(n)$ is obtained from Shih and Hutchinson (1976) assuming plane stress. Note that multiplying the monotonic J_a obtained from ABAQUS, corresponding to a strain amplitude 1.3%, with four, $\Delta J \approx 4J$, the value 140 N mm^{-1} is obtained. This result is equivalent to replacing $\Delta\varepsilon$, $\Delta\sigma$ with $2\varepsilon_a$,

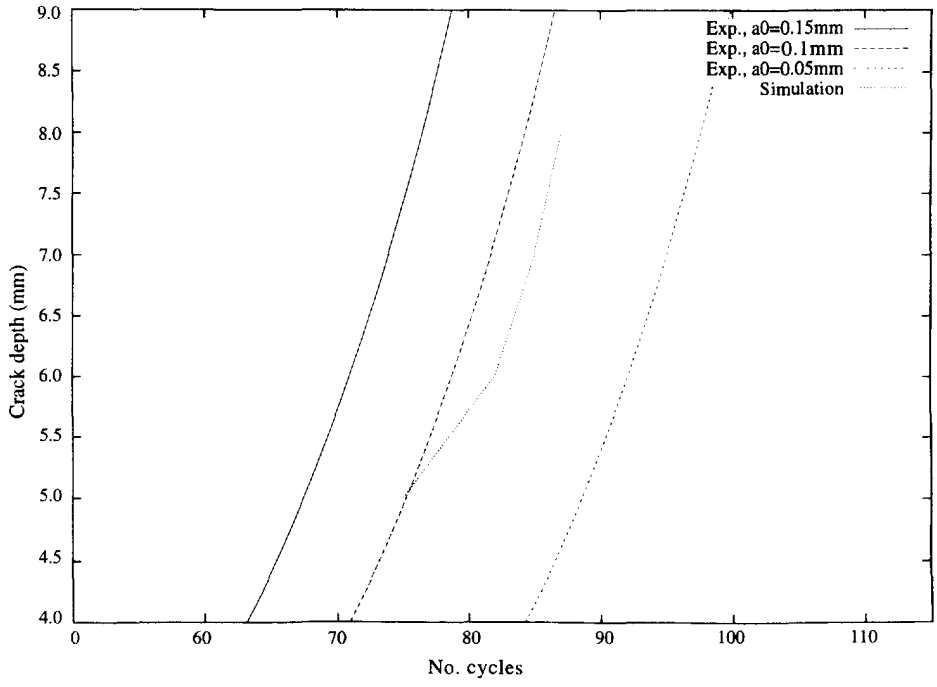

Fig. 15. Comparison of crack depth vs no. cycles in simulation and test.

$2\sigma_a$ in eqn (8). Although the numerically calculated J and estimated J differ, the value determined from ABAQUS is considered to be acceptable.

Correlation to test data

Determining the crack growth rates in the test for $a = 3$, 5, 6, 7 and 8 mm, utilising eqn (19), gives the following results: 0.16, 0.26, 0.32, 0.37 and 0.42 mm cycle^{-1}, respectively. As the steel under consideration is a typical structural steel, representative crack growth in the small scale yielding regime is given as (Barsom, 1971):

$$da/dN = 3.5 \cdot 10^{-12}(\Delta K_J)^3, \text{MPa}\sqrt{\text{m}}, \text{m cycle}^{-1}. \tag{26}$$

Extrapolating this curve into the large scale yielding regime, see Fig. 1(a), and employing the computed ΔJ values to determine ΔK_J, the following fatigue crack growth rates are obtained from eqn (26) for the five crack sizes: 0.02, 0.09, 0.15, 0.24 and 0.39 mm cycle^{-1}. The corresponding tearing crack growth at strain amplitude 0.013 for the five cracks are 0 mm, ≈ 0, 0.05, 0.15 and 0.45 mm, respectively. Hence, the total predicted crack growth rates are 0.02, 0.09, 0.2, 0.39 and 0.84 mm cycle^{-1} by use of eqn (13), i.e. a significant underprediction in crack growth rate for the small cracks and reasonable predictions for $a \geqslant 6$ mm. Crack depth vs number of cycles is plotted in Fig. 15. For the experimental curves, two additional initial crack sizes are utilised in eqn (20) for comparison purposes. From the above results it is observed that the predicted fatigue crack growth is underestimated for $a < 5$ mm. Therefore, in order to compare results where both fatigue and tearing mechanisms are operative in the simulations, the numerical analysis results start at $a = 5$ mm and $N = 75$, assuming that the crack growth up to this magnitude is predicted accurately. Due to the underprediction in fatigue crack growth rate for $a = 5$ mm, the initial slope of the simulation curve is too gentle, but in the last part the curves correspond quite well.

DISCUSSION

Material parameters and characteristic length

As we have mentioned, the determination of the parameters involved in the G–T model is an important, but difficult task. No recommendation for the parameter selection is

available in the literature. By using the methodology proposed by Zhang (1995a), the unknowns and non-uniqueness of the parameters have been reduced. However, there are still unknowns, especially ε_N and s_N, which should depend on the material in question. Nucleation is one of the most difficult problems in the modelling of ductile fracture. Only by close experimental monitoring of the ductile fracture process, can the parameters be accurately determined. Nevertheless, the damage parameters established in this study are in the range of the parameters used in the literature (Sun *et al.*, 1989; Brocks, 1995).

Another open problem in the application of the damage model is the so-called characteristic length. In other words, the material failure usually does not occur when a point in the material has reached the critical value, but when the damage in a volume of material has reached the critical value. In our case, the characteristic length is related to mesh size at the crack tip. It should be mentioned that studying the crack size effect on the ductile tearing is one of our main purposes, rather than accurate prediction of the J_R curves. Different values of the crack growth can be expected if different mesh sizes are used. However, the observation of the crack size effect as well as the three-dimensional effects should be valid.

Crack growth predictions

The maximum J-values (at strain amplitude 0.013) corresponding to crack size 3, 5 and 6 mm are: less than the numerical crack initiation value (J_c), approximately at the initiation value, and above, respectively. This corresponds to the micrographs of the fracture surface showing a slight tendency of ductile damage for $a = 5$ mm and a significant ductile damage development for $a = 7$ mm.

During the cyclic loading, for $a < 5$ mm the fatigue damage mechanism dominates the crack growth. The predicted fatigue crack growth is under-estimated by a factor of 8 and 2.5 for $a = 3$ and 5 mm, respectively. There are several sources for this deviation from the observed behaviour. First, the crack grows through the weld material from the weld root and outwards. The analyses assume homogeneous material in the weld, the real material will exhibit spatial variations both with respect to fatigue crack growth characteristics and stress–strain behaviour. Second, in the ΔJ calculation the cyclic stress–strain behaviour has been simplified by a bi-linear stress–strain curve. The crack growth parameters in the Paris equation (eqn (26)) for the steel will also be an approximation, as it is a mean curve, with typical scatter of ± 2 on crack growth. Thirdly, the way of calculating ΔJ is a simplified method utilising a purely monotonic analysis with the Masing-hypothesis in material behaviour and strain range as input. Although this approach seems to be reasonable, the test for its accuracy is obtained if an implementation of eqn (11) is carried out. Finally, the finite element analyses show that the crack opens near minimum load. Therefore, it is assumed that the full loading branch is contributing to crack growth, i.e. negligible crack closure. This result corresponds to a stationary crack. For the real situation (a growing crack), some actual crack closure variation affecting the fatigue crack growth may, however, be operative, but due to the intense compressive loading, this effect is probably small.

Interaction effects

For $a > 5$ mm the ductile tearing starts to contribute to the crack growth. In our analyses it is assumed that this growth can be determined by analysing the virgin material monotonically and utilising the G–T based constitutive model. Considering a nucleated void in the material in front of the advancing crack tip, the assumption of a spherical shape may be invalidated. A void, initially spherical, may change into an oblate shape during the large compressive loading applied in the analyses. The oblate void could actually approach a penny shaped defect if the compressive loading is large enough. When this void is reloaded in tension, the material around the void is more intensively strained compared to a spherical void. How this may increase damage growth during the load cycling is a topic for future investigations.

In summary, the predicted crack growth by adding up fatigue contributions and ductile crack growth contributions is considered to be in acceptable accordance to the test result. But there is a need for more numerical work on the feasibility of the ΔJ determination, and

experimental work on other materials in order to reveal possible damage interaction that invalidates a simple linear sum of fatigue and tearing crack growth rate.

REFERENCES

Barsom, J. M. (1971). Fatigue crack propagation in steels of various strengths. *Journal of Engineering in Industry, ASME*, **14,** 1190.

Brocks, W. (1995). Numerical round robin on micromechanical models. Fh-IWM report T8/95.

Chell, G. G. (1984). Fatigue crack growth laws for brittle and ductile materials including the effects of static modes and elastic–plastic deformation. *Fatigue Fracture Engineering, Materials and Structures* **7,** 237–250.

Chu, C. C. and Needleman, A. (1980). Void nucleation effects in biaxially stretched sheets. *Journal of Engineering Materials and Technology* **102,** 249–256.

Dowling, N. E. and Begley, J. A. (1976). Fatigue crack growth during gross plasticity and *J*-integral. *ASTM STP* 590, 82–103.

Dowling, N. E. (1978). Crack growth during low cycle fatigue of smooth axial specimens. *ASTM STP* 637, 97–121.

Dowling, N. E. and Iyyer, N. S. (1987). Fatigue crack growth and closure at high cyclic strains. *Materials Science and Engineering* **96,** 99–107.

Franklin, A. G. (1969). Comparison between a quantitative microscopic and chemical method for assessment on non-metallic inclusions. *Journal of the Iron and Steel Institute* **207,** 181–186.

Gurson, A. L. (1977). Continuum theory of ductile rupture by void nucleation and growth: part I—yield criteria and flow rules for porous ductile media. *Journal of Engineering Materials and Technology* **99,** 2–15.

Hibbitt, Karlson and Sorensen. (1992). ABAQUS Theory manual.

Hughes, T. J. R. and Winget, J. (1980). Finite rotation effects in numerical integration of rate constitutive equations arising in large deformation analysis. *International Journal of Numerical Methods in Engineering* **15,** 1862–1867.

Hutchinson, J. (1968). Singular behaviour at the end of a tensile crack in a hardening material. *Journal of Mechanics and Physics of Solids* **16,** 13–31.

Joyce, J. A., Hackett, E. M. and Roe, C. (1994). Effects of cyclic loading on the deformation and elastic plastic fracture behaviour of a cast stainless steel. *ASTM STP* 1202 (Edited by Landes, McCabe and Boulet), pp. 722–744.

Kaiser, S. (1983). On the relation between stable crack growth and fatigue. *Fatigue Fracture Engineering, Materials and Structures* **6,** 33–49.

Koplik, J. and Needleman, A. (1988). Void growth and coalescence in porous plastic solids. *International Journal of Solids and Structures* **124,** 835–853.

Laird, C. and Smith, G. C. (1962). Crack propagation in high stress fatigue. *Philosophical Magazine* **7,** 847–857.

Lambert, Y., Saillard, P. and Bathias, C. (1988). Application of the *J* concept to fatigue crack growth in large scale yielding. *ASTM STP* 969 (Edited by T. A. Cruse), pp. 318–329.

Masing, G. (1926). Eigenspannungen und verfestigung beim messing. *Proceedings of the 2nd International Congress on Applied Mechanics*, Zurich, pp. 332–335.

McClung, R. C. and Hudak, S. J. (1994). Surface crack growth in Inconel 718 during large unload–reload cycles. *ASTM STP* 1202 (Edited by Landes, McCabe and Boulet), pp. 706–721.

McEvily, A. J. (1982). On the quantitative analysis of fatigue crack propagation. *ASTM STP* 811 (Edited by J. Lankford, D. L. Davidson, W. L. Morris and R. P. Wei), pp. 283–312.

Neale, B. K. and Priddle, E. K. (1988). On fatigue crack growth and stable tearing. *Fatigue Fracture Engineering, Materials and Structures* **11,** 31–43.

Neumann, P. (1974). The geometry of slip processes at a propagating fatigue crack—II. *Acta Metallurgica* **22,** 1167–1178.

Paris, P. C. and Erdogan, F. (1963). A critical analysis of crack propagation laws. *Journal of Basic Engineering* **85,** 528–534.

Rice, J. (1967). Mechanics of crack tip deformation and extension by fatigue. *ASTM STP* 415, 247–309.

Rice, J. (1968). A path independent integral and the approximate analysis of strain concentration by notches and cracks. *Journal of Applied Mechanics* **35,** 379–386.

Rice, J. and Rosengren, G. F. (1968). Plane-strain deformation near a crack tip in a power law hardening material. *Journal of Mechanics and Physics of Solids* **16,** 1–12.

Roven, H. J. and Nes, E. (1991). Cyclic deformation of ferritic steel—II, stage II crack propagation. *Acta Metallurgica Mater.* **39,** 1735–1754.

Shih, C. F. (1981). Relationships between the *J*-integral and the crack opening displacement for stationary and opening cracks. *Journal of Mechanics and Physics of Solids* **29,** 305–326.

Shih, C. F. and Hutchinson, J. W. (1976). Fully plastic solutions and large scale yielding estimates for plane stress crack problems. *Journal of Engineering and Materials Technology* **98,** 289–295.

Skallerud, B. (1992a). On the relationship between low cycle fatigue and crack growth rate properties in welded steel components. *Fatigue Fracture Engineering, Materials and Structures* **15,** 43–56.

Skallerud, B. (1992b). Constitutive modelling of cyclic plasticity and some implications for the computation of biaxial low cycle fatigue. *Engineering Fracture Mechanics* **41,** 753–769.

Skallerud, B., Amdahl, J., Eide, O. I. and Johansen, A. (1995). On the capacity of tubular T-joints subjected to severe cyclic loading. *Proceedings of Offshore Mechanics and Arctic Engineering (OMAE)*, Copenhagen, Vol. 1B, pp. 133–143.

Sun, D. Z., Siegele D., Voss, B. and Schmitt, W. (1989). Application of local damage models to the numerical analysis of ductile rupture. *Fatigue Fracture Engineering, Materials and Structures* **12,** 210–212.

Tanaka, K. (1989). Mechanics and micromechanics of fatigue crack propagation. *ASTM STP* 1020 (edited by R. P. Wei and R. P. Gangloff), pp. 151–183.

Thomason, P. F. (1989). *Ductile Fracture of Metals*. Pergamon Press, London.
Tvergaard, V. (1981). Influence of voids on shear band instabilities under plane strain conditions. *International Journal of Fracture* **17,** 389–407.
Tvergaard, V. (1982). On localization in ductile materials containing spherical voids. *International Journal of Fracture* **18,** 237–252.
Tvergaard, V. and Needleman, A. (1984). Analysis of the cup-cone fracture in a round tensile bar. *Acta Metallurgica* **32,** 157–169.
Xia, L. and Shih, C. F. (1995). Ductile crack growth—I. A numerical study using computational cells with microstructurally based length scales. *Journal of Mechanics and Physics of Solids* **43,** 233–259.
Yoon, K. B. and Saxena, A. (1991). An interpretation of ΔJ for cyclically unsaturated materials. *International Journal of Fracture* **49,** 3–9.
Zhang, Z. L. (1995a). A methodology for determining the Gurson parameters (in preparation).
Zhang, Z. L. (1995b). Explicit consistent tangent moduli with a return mapping algorithm for pressure-dependent elastoplasticity models. *Computational Methods in Applied Mechanical Engineering* **121,** 29–44.
Zhang, Z. L. and Niemi, E. (1995a). A new failure criterion for the Gurson–Tvergaard dilatational constitutive model. *International Journal of Fracture* **70,** 321–334.
Zhang, Z. L. and Niemi, E. (1995b). A class of generalised mid-point algorithms for the Gurson–Tvergaard material model. *International Journal of Numerical Methods in Engineering* **38,** 2033–2053.